fluids

MDPI

Article

Hydrodynamic Regulation and Gas–Liquid Mass Transfer in a Spatially Configured Multiscale Bubble Distributor

Luhaibo Zhao [1,2,*] and Jiarui Xu [2,3]

[1] Department of Mechanics, Shanghai Institute of Applied Mathematics and Mechanics, School of Mechanics and Engineering Science, Shanghai University, Shanghai 200444, China
[2] Shanghai Advanced Research Institute, Chinese Academy of Sciences, Shanghai 201210, China
[3] School of Energy and Power Engineering, University of Shanghai for Science and Technology, Shanghai 200093, China
* Correspondence: zhaolhb@shu.edu.cn

Abstract

An experimental investigation was conducted in a bubble column to clarify how bubble-source composition and spatial configuration regulate multiscale bubble dynamics and gas–liquid mass transfer. A combined bubble distributor containing different pore-size generators and adjustable vertical arrangements was developed to regulate bubble-source composition and spatial configuration. The final bubble size was found to result from continuous generation, transport, collision/coalescence, and size redistribution rather than from sparger pore size alone. Small- and large-scale bubbles exhibited clearly differentiated hydrodynamic characteristics; in particular, the Weber number of large-scale bubbles ranged from 0.44 to 2.02, indicating a stronger competition between inertia and surface tension and a greater potential for interfacial renewal. Convex configurations generally favored large-scale-bubble transport, whereas concave configurations enhanced small-scale-bubble retention and interfacial-area preservation. The experimental results demonstrate that mass-transfer enhancement arises from the coordinated balance between bubble-population structure and hydrodynamic renewal rather than from maximizing a single bubble parameter.

Keywords: combined bubble distributor; multiscale bubbles; bubble column; gas–liquid mass transfer; high-speed visualization

1. Introduction

Gas–liquid two-phase flows are widely encountered in chemical reaction engineering, biochemical processing, energy conversion, and wastewater treatment, where gas–liquid mass transfer often plays a decisive role in reactor performance [1–4]. In bubble columns and related reactors, bubble size, rise velocity, spatial distribution, and swarm interactions directly affect gas holdup, interfacial area, liquid circulation, and mass-transfer behavior [5–8]. Bubble dynamics and interfacial transport are therefore strongly coupled.

Reducing bubble size is a common strategy for enhancing mass transfer because smaller bubbles provide larger specific interfacial area, lower rise velocity, and longer gas–liquid contact time [9–11]. However, larger bubbles exhibit stronger buoyancy and inertial effects, which promote interfacial deformation, liquid motion, and wake development [5,12,13]. Thus, small and large bubbles provide different but potentially complementary functions: small-scale bubbles favor interfacial-area preservation, whereas large-scale bubbles enhance hydrodynamic renewal. Practical bubble columns often exhibit broad

Check for updates

Academic Editor: Lixin Cheng

Received: 15 September 2026
Revised: 9 October 2026
Accepted: 13 October 2026
Published: 22 October 2026

Copyright: © 2026 by the authors. Licensee MDPI, Basel, Switzerland. This article is an open access article distributed under the terms and conditions of the Creative Commons Attribution (CC BY) license.

or multimodal bubble-size distributions. During transport, bubble collision, coalescence, breakup, and migration continuously reshape the bubble population [14,15]. As a result, multiscale bubble systems cannot be adequately characterized by a single mean diameter or total gas holdup; the relative populations, velocities, and spatial organization of different bubble scales must also be considered. The gas distributor determines the initial conditions of bubble generation. Sparger type, aperture size, and spatial arrangement can substantially affect bubble-size and rise-velocity distributions, gas holdup, and flow-regime development [16–19]. Kulkarni and Joshi demonstrated the strong dependence of bubble-column performance on sparger design [16], while tomographic and experimental studies further showed that different distributor structures produce different gas-holdup and bubble-size distributions [17,18]. More recently, Yao et al. showed that distributor aperture size and spatial arrangement influence both bubble-scale behavior and reactor-scale hydrodynamics [19]. For a combined distributor containing units with different pore sizes, the final bubble population cannot be regarded as a simple superposition of bubbles generated from individual pores. After detachment, bubbles undergo migration, collision, coalescence, and possible breakup, causing continuous redistribution of bubble size and velocity [14,15]. Therefore, the nominal pore size mainly defines the initial bubble-generation condition rather than the final bubble scale in the bulk flow. High-speed visualization and image-based analysis now provide quantitative tools for characterizing complex bubbly flows. Conventional image-processing methods can extract bubble size, shape, velocity, and trajectory [20,21], while recent deep-learning approaches have improved bubble detection and reconstruction under overlapping and dense conditions [22–25]. In our previous work, a YOLOv8-based real-time framework was established for simultaneous measurement of multiscale bubble size and velocity together with gas–liquid mass-transfer analysis [26].

On this basis, the present study develops a combined bubble distributor with different pore-size units and adjustable vertical arrangements. The effects of bubble-source composition and spatial configuration on bubble-size redistribution, bubble velocity, scale-dependent hydrodynamics, and gas–liquid mass transfer are systematically investigated. The objective is to clarify how spatially regulated multiscale bubble populations balance interfacial-area preservation by small-scale bubbles and hydrodynamic renewal by large-scale bubbles, thereby establishing a structure–dynamics–mass-transfer framework for multiscale gas–liquid reactors.

2. Experimental Setup and Methods

2.1. Combined Bubble Distributor and Experimental System

The multiscale bubble experiments were conducted in a self-built transparent rectangular bubble column, as shown in Figure 1. The column was made of transparent Perspex to allow visualization of bubble generation, transport, and swarm evolution. Deionized water at room temperature was used as the liquid phase, and all experiments were performed under atmospheric pressure. Air supplied by an air compressor was regulated through a pressure-stabilizing unit and independently controlled by rotameters before entering the bubble-generating units. A combined bubble distributor composed of metal membrane units with nominal pore sizes of 2 μm and 10 μm was installed at different vertical positions in the column. The pore size represents the characteristic scale of the bubble-generating source rather than the final bubble diameter. After detachment from the distributor, bubbles undergo migration, collision, coalescence, and possible breakup, resulting in continuous redistribution of the bubble-size population during upward transport. Therefore, the combined distributor was used to regulate the initial bubble-source composition and spatial arrangement, rather than to directly prescribe the final bubble size. Different multiscale

bubble populations were generated by independently controlling the gas flow rate and spatial arrangement of the individual bubble-generating units.

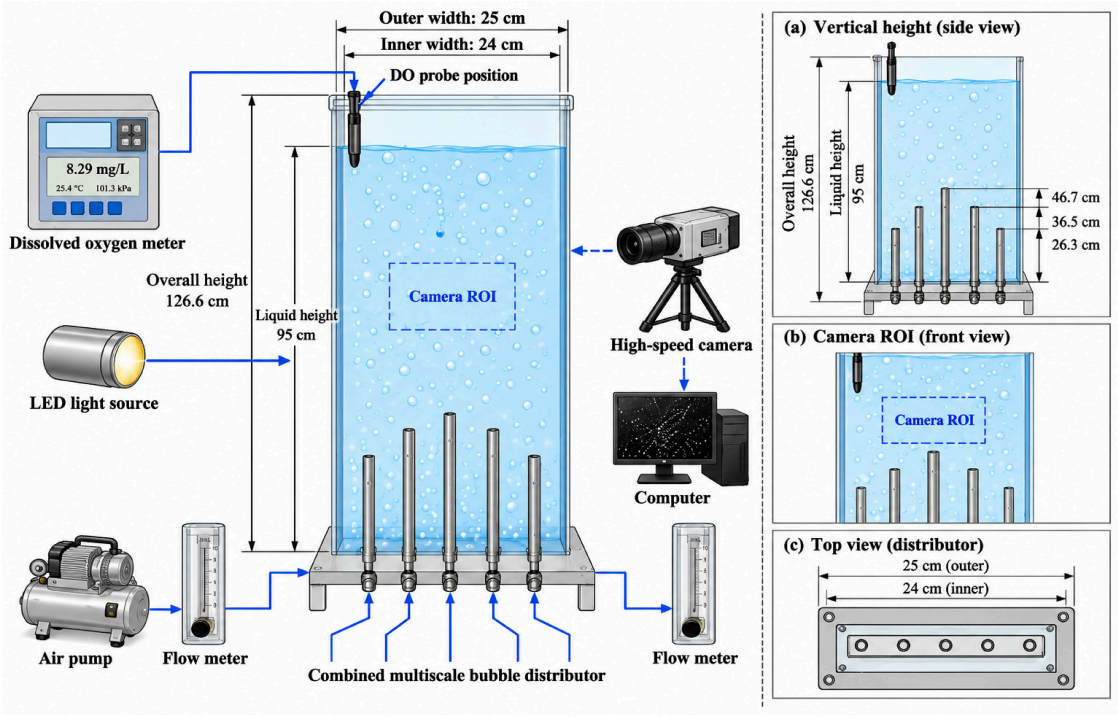


Figure 1. Schematic of the combined multiscale bubble experimental system and measurement configuration.

Bubble motion was recorded using a high-speed visualization system consisting of a Revealer 5KF20G high-speed camera, a macro lens, an LED backlight, and a diffusion plate. The camera has a resolution of 1920 × 1080 pixels and was operated at 1000 fps, with an exposure time of 300 µs. The diffusion plate was placed between the light source and the bubble column to improve illumination uniformity and enhance bubble-boundary recognition. The acquired images were subsequently processed using the previously developed multiscale bubble visualization method to obtain bubble-size and velocity statistics under different operating conditions.

2.2. Bubble Visualization Measurement Method

To quantitatively characterize the bubble population generated by the combined distributor, the deep-learning-based visualization method developed in our previous work was employed for bubble detection, tracking, and simultaneous extraction of bubble size and velocity [26]. The method enables automated identification of individual bubbles in complex bubbly flows and provides statistical information on bubble size and motion.

The bubble size was quantified using the projected-area-based equivalent diameter, which is commonly used in optical measurements of bubbly flows [5,26]. Since the present study focuses on statistical comparison among different distributor configurations, the same imaging geometry and size-conversion procedure were applied to all experimental cases. The equivalent bubble diameter was calculated from the projected bubble area as:

$$d_{eq} = \sqrt{\frac{4A_p}{\pi}} \quad (1)$$

where A_p is the two-dimensional projected area of the detected bubble. The camera system was calibrated using a reference scale, giving a spatial resolution of approximately 40 µm/pixel. Considering a conservative one-pixel uncertainty in contour localization, the

corresponding resolution-related diameter uncertainty was estimated to be approximately 0.08 mm. Additional systematic uncertainty associated with the two-dimensional projection of deformed bubbles cannot be completely eliminated. Because the instantaneous three-dimensional orientation and shape of deformed bubbles were not measured, this projection-related component cannot be uniquely quantified from the present two-dimensional images and is therefore treated as a systematic limitation rather than being included in the 0.08 mm resolution-related estimate. Although the relative influence of image resolution increases for smaller bubbles, the same imaging geometry, calibration procedure, and image-processing method were applied to all experimental conditions, providing a consistent basis for comparative statistical analysis among different configurations.

Based on the measured bubble-size distributions, d_{eq} = 1.0 mm was adopted as an operational criterion to distinguish small-scale and large-scale bubbles. This classification was adopted to distinguish the hydrodynamic behaviors of the two bubble populations rather than to establish a direct correspondence with the nominal pore sizes of the bubble generators. This criterion was used for scale-resolved statistical analysis and was not intended to represent a universal physical boundary between bubble regimes. Similar distinctions between sub-millimeter and millimeter-scale bubbles have also been widely discussed in gas–liquid systems [27,28]. From a hydrodynamic perspective, sub-millimeter bubbles are generally characterized by stronger surface-tension effects, relatively limited deformation, and higher interfacial-area preservation potential, whereas millimeter-scale bubbles experience stronger buoyancy and inertial effects, leading to enhanced deformation, wake interaction, and interfacial renewal. Therefore, the 1 mm criterion in the present study represents the transition between two experimentally observed bubble populations with different hydrodynamic characteristics rather than an imposed universal cutoff.

The bubble velocity was obtained from the displacement of the detected bubble centroid between successive tracked frames:

$$U_b = \frac{\Delta s}{\Delta t} \tag{2}$$

where Δs is the centroid displacement after spatial calibration and Δt is the corresponding time interval. The resulting bubble-size and velocity data were used to characterize scale-dependent bubble transport and to calculate the Reynolds, Weber, and Eötvös numbers.

2.3. Mass Transfer Performance Measurement

The gas–liquid mass-transfer performance was characterized by the volumetric mass-transfer coefficient k_La, which was determined using the dynamic dissolved-oxygen method. Nitrogen was first introduced into the column to reduce the dissolved oxygen concentration. After a sufficiently low and stable oxygen level was reached, the gas supply was switched to air, and the temporal variation in dissolved oxygen concentration was recorded.

Assuming a well-mixed liquid phase, the oxygen mass balance can be expressed as

$$\frac{dC}{dt} = k_La(C^* - C) \tag{3}$$

where C is the instantaneous dissolved oxygen concentration and C^* is the saturation concentration. Integration gives

$$\ln\left(\frac{C^* - C_0}{C^* - C}\right) = k_La\ t \tag{4}$$

where C_0 is the dissolved oxygen concentration at the beginning of aeration. The experimental k_La was obtained from the slope of the linear fitting curve. Here, k_L is the liquid-side

mass-transfer coefficient and a is the specific gas–liquid interfacial area. For a bubble population, the interfacial area can be estimated as

$$a = \frac{6\varepsilon_g}{d_{32}} \tag{5}$$

where ε_g is the gas holdup and d_{32} is the Sauter mean bubble diameter. For the small- and large-scale bubble populations, the corresponding quantities are expressed as

$$a_j = \frac{6\varepsilon_j}{d_{32,j}}, j = s, l. \tag{6}$$

The scale-resolved volumetric mass-transfer coefficient can then be written as

$$(k_L a)_j = k_{L,j}\, a_j,\ j = s, l. \tag{7}$$

The scale-resolved gas holdups, ε_s and ε_l, were determined from the image-based bubble population statistics following the procedure established in our previous work [26], with $\varepsilon_g = \varepsilon_s + \varepsilon_l$. To evaluate the scale-dependent mass-transfer contribution, the liquid-side mass-transfer coefficient was estimated using Higbie's penetration theory [29]:

$$k_L = \frac{2}{\sqrt{\pi}}\sqrt{\frac{D_L U_{\text{slip}}}{d_b}} \tag{8}$$

where D_L is the molecular diffusivity of oxygen in water, U_{slip} is the bubble–liquid slip velocity, and d_b is the characteristic bubble diameter. Under the present experimental conditions, the liquid bulk velocity was relatively small compared with the bubble rise velocity, and U_{slip} was approximated by the measured bubble velocity U_b. The Higbie penetration model was adopted because it provides a direct coupling between bubble size, slip velocity, and interfacial renewal. In our previous study using the same experimental system, several commonly used k_L correlations were compared with dynamic dissolved-oxygen measurements, and the Higbie-based prediction showed the closest overall agreement [26]. Nevertheless, the applicability of this model depends on bubble interfacial mobility. Small or partially contaminated bubbles may exhibit reduced surface mobility and approach rigid-interface behavior, for which Frössling-type correlations are more appropriate [30]. Therefore, the present k_L calculations are primarily used for comparative evaluation of scale-dependent mass-transfer contributions among different configurations rather than as universal absolute predictions for all bubble sizes.

The total volumetric mass-transfer coefficient was decomposed into the contributions of small- and large-scale bubble populations:

$$(k_L a)_{\text{total}} = (k_L a)_s + (k_L a)_l \tag{9}$$

and their relative contributions were defined as

$$\eta_s = \frac{(k_L a)_s}{(k_L a)_{\text{total}}} \tag{10}$$

$$\eta_l = \frac{(k_L a)_l}{(k_L a)_{\text{total}}} \tag{11}$$

This scale-resolved analysis was combined with the measured bubble-size and velocity distributions to examine how the spatial configuration regulates the balance

between interfacial-area preservation by small-scale bubbles and hydrodynamic renewal by large-scale bubbles.

3. Effect of Distributor Spatial Configuration on Multiscale Bubble Characteristics and Gas–Liquid Mass Transfer Performance

3.1. Bubble Source Combinations and Spatial Configurations

To investigate the effects of bubble-source composition and spatial arrangement on multiscale bubble-swarm dynamics, the previous dual-source distributor was modularly extended to five independently controlled bubble-generating positions, as shown in Figure 2. The five positions were arranged laterally in the sequence 2–10–2–10–2 μm, and their vertical locations were adjusted using connecting tubes of different lengths. By independently controlling the vertical position and on/off state of each unit, different initial bubble-source distributions and gas-input conditions were established. According to the relative vertical positions of the five bubble-generating units, two basic spatial configurations were defined: convex and concave. In the convex configurations (a–d), the source heights were 0.2–0.3–0.4–0.3–0.2 m, with the central source positioned highest, forming a peak-like arrangement. In the concave configurations (e–h), the corresponding heights were 0.4–0.3–0.2–0.3–0.4 m, with the central source positioned lowest, forming a valley-like arrangement. The two configuration types had the same lateral pore-size sequence and differed only in the relative vertical positions of the sources, allowing the influence of source height and bubble-rise-path interaction on swarm transport and bubble-size evolution to be examined.

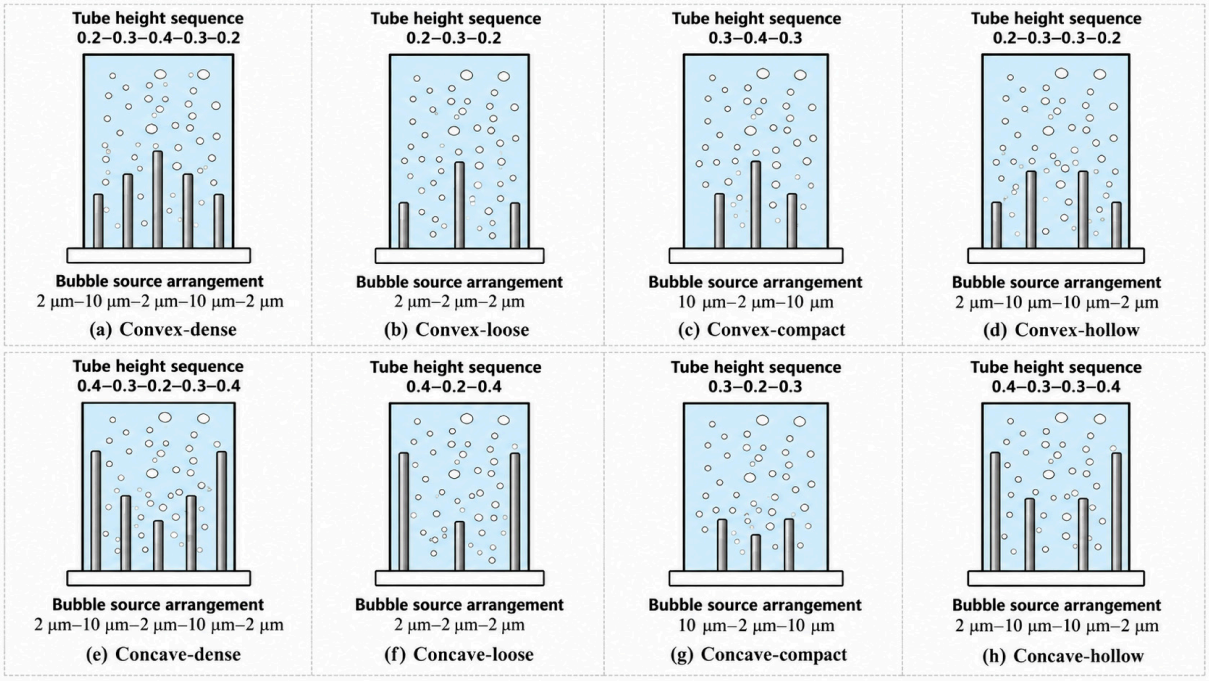


Figure 2. Bubble-source combinations and spatial configurations of the combined distributor.

Within each spatial configuration, four bubble-source combinations—dense, loose, compact, and hollow—were generated by changing the on/off states of the five units, resulting in eight experimental conditions in total. The corresponding gas-flow conditions are summarized in Table 1. It should be noted that comparisons between paired convex and concave cases isolate the effect of spatial arrangement more directly, whereas comparisons among the four source combinations also involve changes in the active-source composition and total gas input.

Table 1. Gas flow control parameters of the combined bubble column.

Bubble Generation Unit	Convex Dense	Convex Loose	Convex Compact	Convex Hollow	Concave Dense	Concave Loose	Concave Compact	Concave Hollow
Position 1 (2 μm) Flow rate/(L/min)	0.3	0.3	0	0.3	0.3	0.3	0	0.3
Position 2 (10 μm) Flow rate/(L/min)	0.5	0	0.5	0.5	0.5	0	0.5	0.5
Position 3 (2 μm) Flow rate/(L/min)	0.3	0.3	0.3	0	0.3	0.3	0.3	0
Position 4 (10 μm) Flow rate/(L/min)	0.5	0	0.5	0.5	0.5	0	0.5	0.5
Position 5 (2 μm) Flow rate/(L/min)	0.3	0.3	0	0.3	0.3	0.3	0	0.3

3.2. Bubble Size Distribution

Figure 3 shows representative bubble images and the corresponding equivalent-diameter distributions under the eight combined-distributor conditions. All cases exhibit clear multiscale characteristics, with bubble sizes spanning from the sub-millimeter to several-millimeter range. However, the dominant peak, distribution width, and fraction of small-scale bubbles vary among configurations, indicating that the final bubble population is not directly determined by sparger pore size but evolves through a continuous process of initial generation, spatial transport, collision/coalescence, and size redistribution. Quantitatively, the characteristic diameters of the small-scale bubble population are approximately 0.63–0.81 mm, whereas those of the large-scale population are approximately 1.92–2.26 mm. The separation between these two characteristic size ranges supports the use of 1.0 mm as an operational criterion for the subsequent scale-resolved analysis. The images shown in Figure 3 are representative examples for visual assessment, while the quantitative recognition accuracy was evaluated independently using 200 manually labeled bubbles as described below.

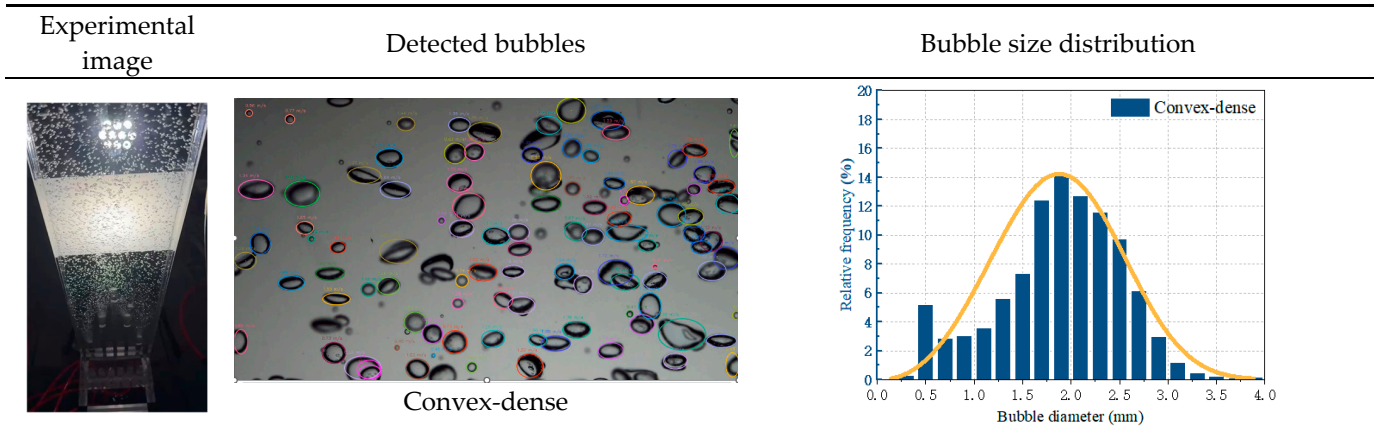


Figure 3. *Cont.*

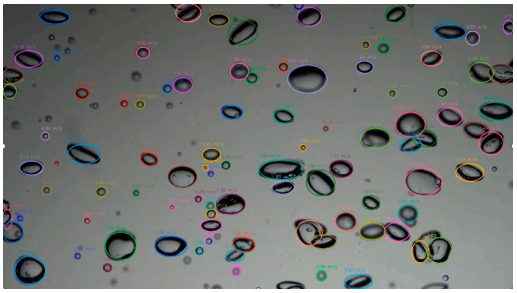
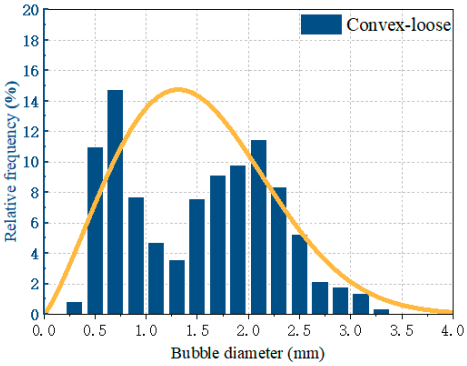
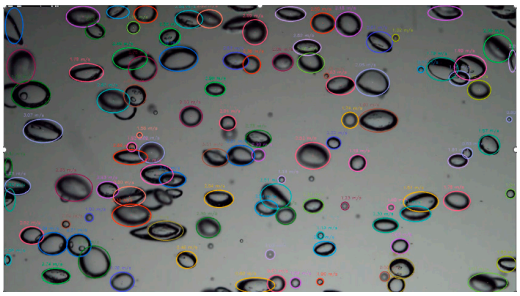
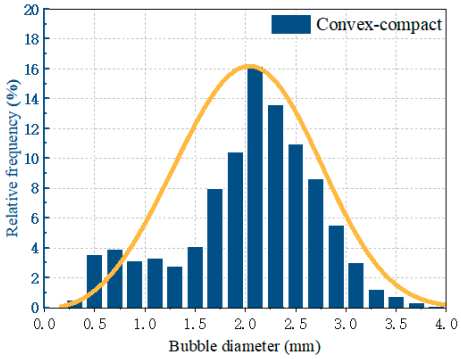
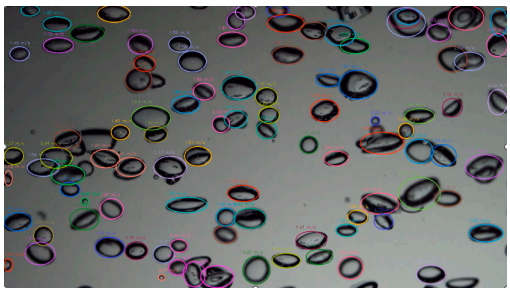
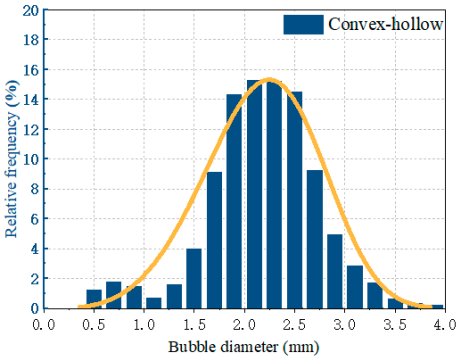
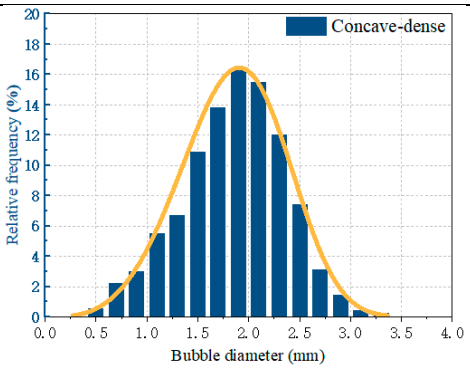
Experimental image	Detected bubbles	Bubble size distribution
	 Convex-loose	
	 Convex-compact	
	 Convex-hollow	
	 Concave-dense	

Figure 3. *Cont.*

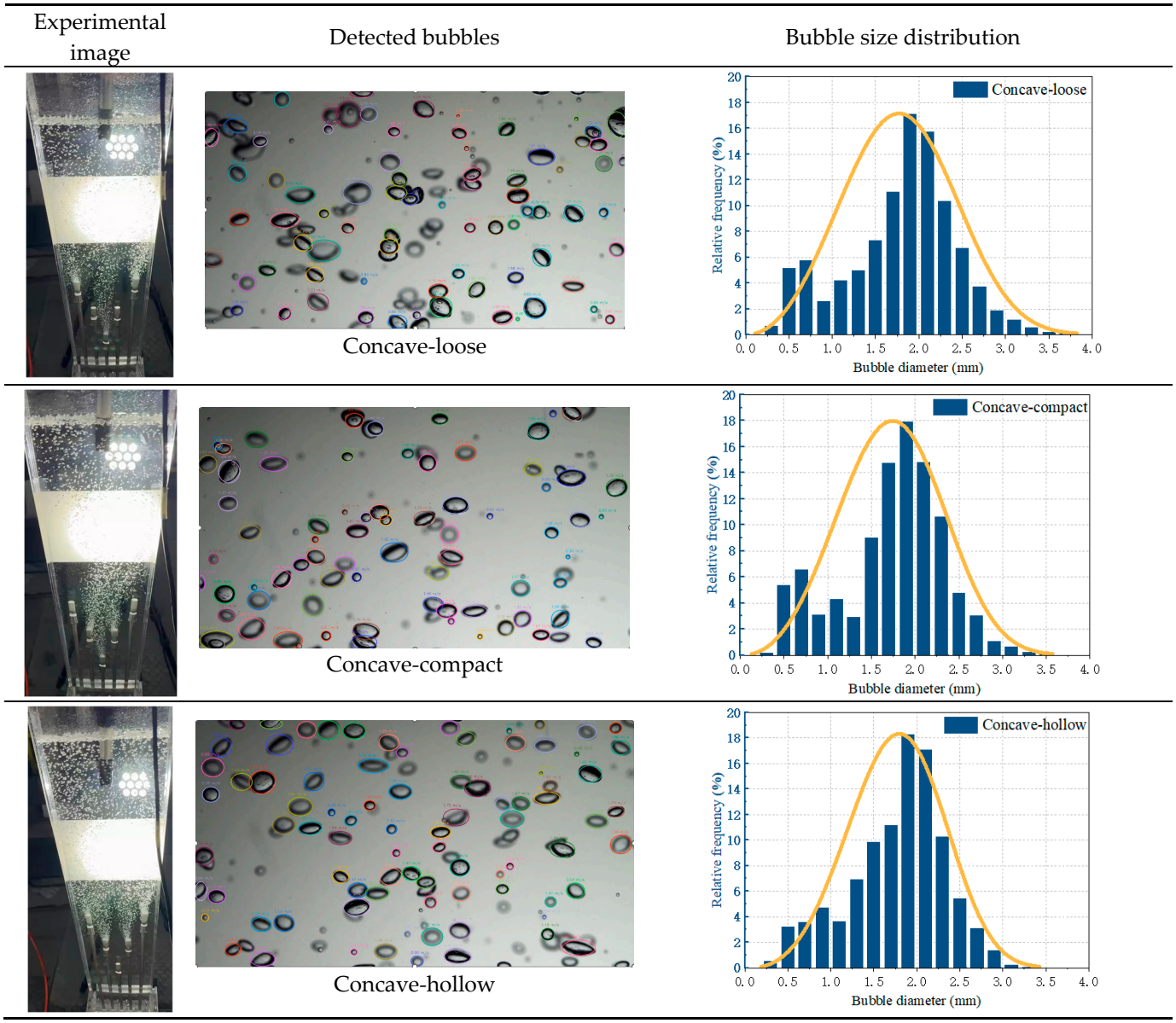


Figure 3. Bubble images, detection results, and size distributions under different configurations. The yellow curves represent kernel-density estimates used to guide visualization of the bubble-size distributions.

To evaluate the reliability of the image-based bubble measurement, the detected contours were quantitatively compared with manually labeled bubble boundaries. A total of 200 bubbles were randomly selected from the present experimental images for validation, covering the investigated configurations and including both small- and large-scale bubbles. The contour agreement was evaluated using the intersection-over-union (IoU) metric, while the relative equivalent-diameter deviation was calculated as

$$\delta_d = \frac{|d_{AI} - d_{manual}|}{d_{manual}} \times 100\% \tag{12}$$

where d_{AI} and d_{manual} represent the equivalent diameters obtained from the automatically detected and manually labeled contours, respectively. The average IoU was 0.90 ± 0.04, and the mean absolute relative equivalent-diameter deviation was approximately 2.0%, with a standard deviation of approximately 1.5%. Here, the value of 1.5% represents the standard deviation of the sample-wise equivalent-diameter deviations rather than the

recognition error itself. It should also be noted that the local contour discrepancies visible in Figure 3 and the equivalent-diameter deviation characterize different aspects of recognition performance. IoU reflects contour-level agreement, whereas d_{eq} is calculated from the total projected bubble area and is therefore less sensitive to localized contour deviations. Consequently, a visually noticeable local contour mismatch does not necessarily produce a comparable percentage error in equivalent diameter. The camera system was calibrated using a reference scale, giving a spatial resolution of approximately 40 µm/pixel. Considering a conservative one-pixel uncertainty in contour localization, the corresponding resolution-related diameter uncertainty was estimated to be approximately 0.08 mm. This resolution-related estimate and the experimentally evaluated AI–manual diameter deviation represent different uncertainty components and should not be directly compared. To further verify the agreement between the automated and manual measurements over the full validation dataset, Figure 4 compares d_{AI} and d_{manual} for all 200 bubbles.

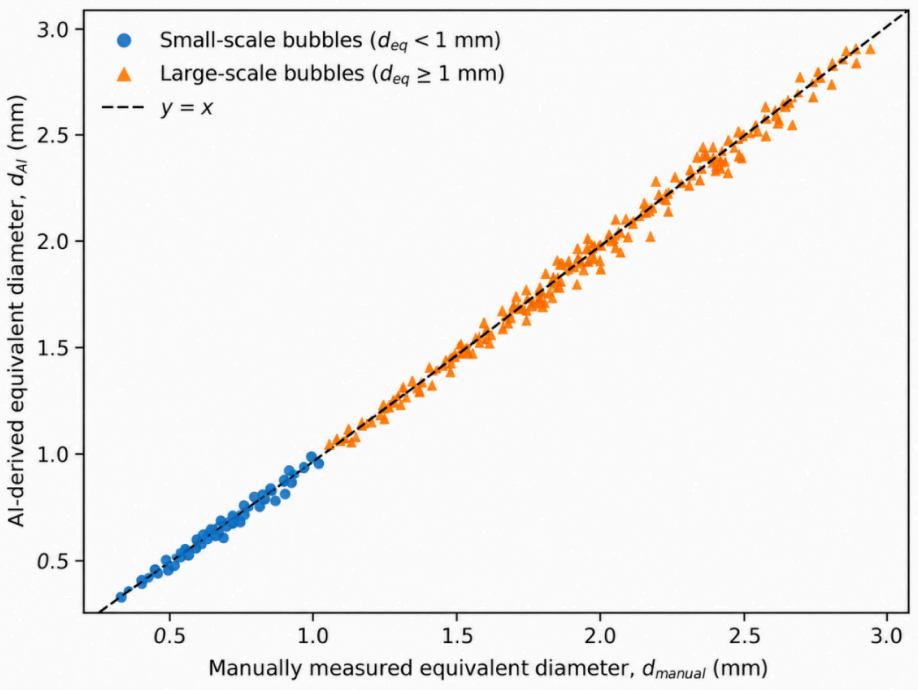


Figure 4. Comparison between AI-derived and manually measured equivalent bubble diameters for the 200 validation bubbles. The dashed diagonal line represents $d_{AI} = d_{manual}$. Small- and large-scale bubbles are classified using the manually determined equivalent diameter according to the operational criterion d_{eq} = 1 mm.

The validation was performed under the same camera settings, spatial calibration, illumination conditions, and image-processing procedure as those used throughout the present experiments. Therefore, the reported validation statistics characterize the performance of the present image-analysis procedure under the investigated experimental conditions and should not be interpreted as universal quantitative validation under arbitrary imaging, illumination, or severe bubble-overlap conditions. Although two-dimensional projection may introduce additional uncertainty for deformed bubbles, the same imaging and size-conversion procedure was consistently applied to all configurations, providing a consistent basis for comparative analysis.

Overall, the combined distributor regulates bubble size through a coupled generation–transport–interaction–redistribution process. The pore-size combination and gas input determine the initial bubble-source conditions, while the spatial arrangement further modifies swarm interaction and the resulting size spectrum. Therefore, the regulation of a

multiscale bubble system should be evaluated not only by mean bubble size, but also by the distribution width and the relative fractions of different bubble scales.

3.3. Bubble Velocity Distribution

Figure 5 presents the bubble velocity distributions under the eight combined-distributor configurations. Clear differences are observed in the peak position, distribution width, and fraction of high-velocity bubbles, indicating that bubble transport is jointly affected by bubble size, bubble-source composition, spatial arrangement, and swarm interactions. Compared with the corresponding concave cases, the convex configurations generally exhibit broader or higher-velocity distributions, whereas the concave configurations tend to show more concentrated medium-to-low velocity ranges.

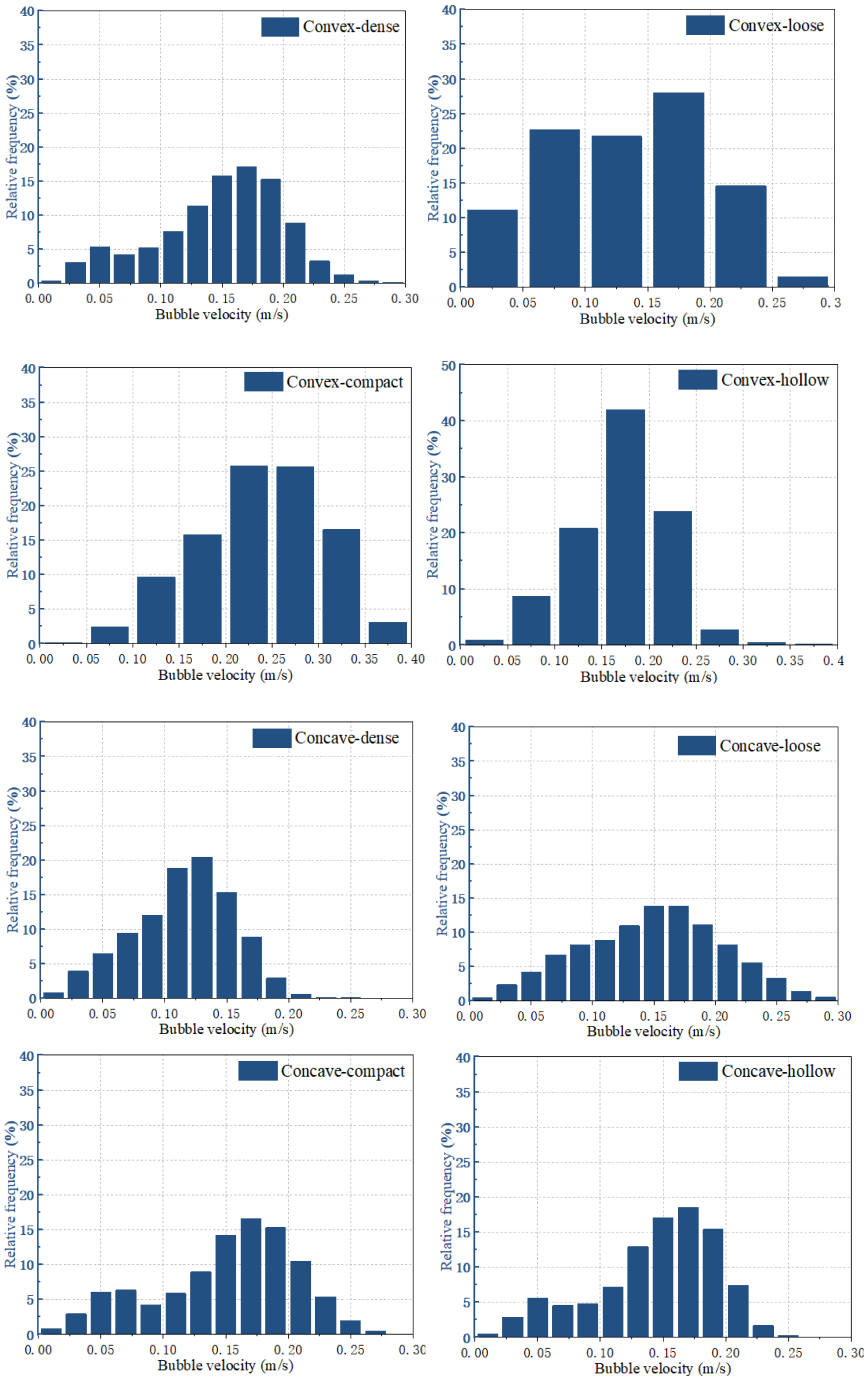


Figure 5. Histograms of bubble velocity distributions under different configurations.

Among the eight cases, the convex-compact configuration exhibits the most pronounced shift toward higher velocities, with the main bubble population concentrated in the high-velocity range and extending to the highest velocities observed in the experiments. In contrast, the concave-compact case remains mainly in the medium-velocity range despite having the same source composition and gas input. A similar convex–concave difference is observed for the dense and hollow pairs, while the concave-dense case shows the lowest overall velocity level. These paired comparisons demonstrate that changing only the relative vertical positions of the bubble sources can substantially alter the bubble-swarm transport state. Overall, the effect of spatial configuration is reflected primarily in the redistribution and broadening of the velocity spectrum rather than in a uniform increase or decrease in bubble velocity. Moreover, bubble velocity does not vary monotonically with total gas flow rate, indicating that axial transport is governed by the combined effects of bubble-size evolution, source composition, and spatial organization. The convex-compact case represents the strongest axial transport state, whereas the concave-dense case exhibits comparatively weaker bubble transport. This trend is consistent with the corresponding size distributions, suggesting that bubble-size evolution and transport velocity respond jointly to the spatial configuration.

3.4. Dimensionless Parameters and Multiscale Bubble Dynamics

The mean bubble diameter and rise velocity under different configurations are shown in Figure 6 and error bars represent ±SD of the detected bubble population. To characterize the scale-dependent hydrodynamic states, the Reynolds number Re_b, Weber number We, and Eötvös number Eo were calculated from the measured equivalent diameter d_b and mean rise velocity U_b:

$$Re_b = \frac{\rho_l U_b d_b}{\mu_l}, We = \frac{\rho_l U_b^2 d_b}{\sigma}, Eo = \frac{(\rho_l - \rho_g) g d_b^2}{\sigma}, \quad (13)$$

where ρ_l and ρ_g are the liquid and gas densities, μ_l is the liquid dynamic viscosity, σ is the gas–liquid interfacial tension, and g is the gravitational acceleration. The dimensionless parameters for the small- and large-scale bubble populations are summarized in Table 2.

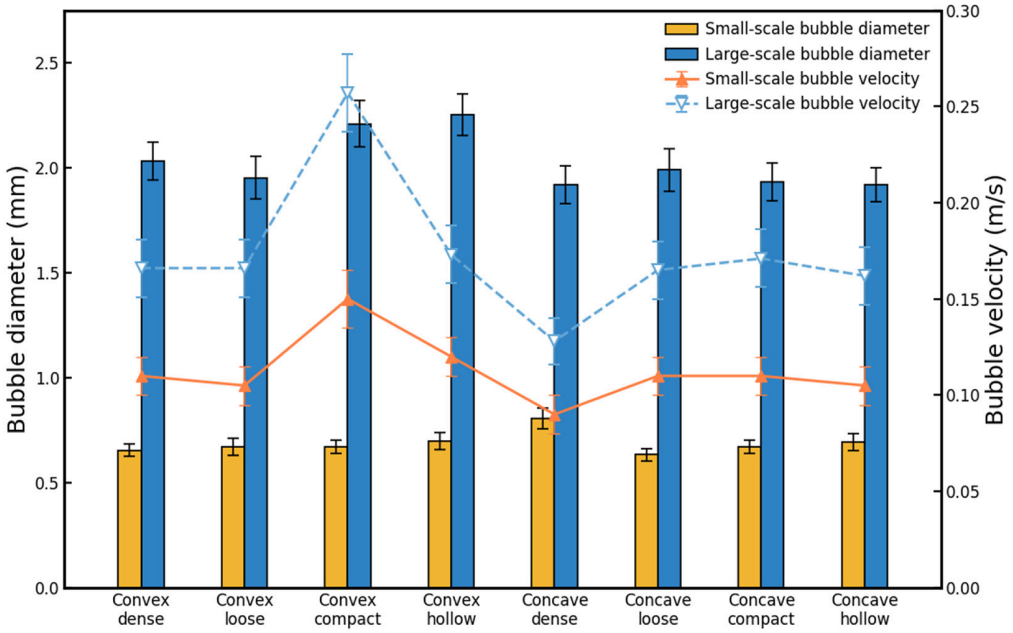


Figure 6. Mean bubble diameter and velocity under different configurations.

Table 2. Dimensionless hydrodynamic parameters of multiscale bubbles.

Configuration	Re_s	We_s	Eo_s	Re_l	We_l	Eo_l
Convex-dense	80	0.109	0.058	378	0.775	0.560
Convex-loose	79	0.103	0.061	363	0.745	0.517
Convex-compact	113	0.209	0.061	636	2.020	0.662
Convex-hollow	94	0.139	0.066	437	0.934	0.689
Concave-dense	81	0.090	0.088	275	0.436	0.500
Concave-loose	78	0.106	0.054	368	0.750	0.537
Concave-compact	83	0.112	0.061	370	0.783	0.507
Concave-hollow	82	0.106	0.066	348	0.697	0.499

The two bubble populations occupy clearly different hydrodynamic ranges. Small-scale bubbles exhibit $Re_s \approx 78$–113, $We_s \approx 0.09$–0.21, and $Eo_s \approx 0.054$–0.088. The low We_s and Eo_s values indicate that surface tension strongly constrains interfacial deformation, while inertia is sufficient to sustain bubble transport but remains relatively limited. Consequently, the small-scale bubbles maintain comparatively stable interfaces and are favorable for preserving effective gas–liquid interfacial area. Large-scale bubbles exhibit higher $Re_l \approx 275$–636, $We_l \approx 0.44$–2.02, and $Eo_l \approx 0.50$–0.69. The increases in all three parameters indicate enhanced inertial and buoyancy effects relative to the small-scale population. In particular, We_l approaches or exceeds unity in several configurations, indicating a greater potential for interfacial deformation and wake-related disturbance. Thus, large-scale bubbles exhibit stronger transport and interfacial-renewal potential, whereas small-scale bubbles remain more strongly constrained by surface tension. The spatial configuration further modifies these hydrodynamic states. The convex-compact configuration exhibits the highest large-scale values, with $Re_l \approx 636$ and $We_l \approx 2.02$, consistent with its comparatively high-rise velocity and strongest axial transport among the investigated cases. In contrast, the concave-dense configuration shows the lowest large-scale Re_l and We_l, indicating weaker inertial transport. These results demonstrate that the combined distributor regulates bubble dynamics through the coupled modification of bubble size and velocity, thereby altering the relative roles of inertia, viscosity, buoyancy, and surface tension.

The scale-dependent hydrodynamic differentiation provides a physical basis for the different mass-transfer roles of the two bubble populations. Small-scale bubbles exhibit relatively low *Re*, *We*, and *Eo*, with $We < 1$ and $Eo \ll 1$. These values indicate that surface tension strongly constrains interfacial deformation, while buoyancy remains comparatively weak. Therefore, small-scale bubbles tend to maintain relatively stable interfaces and contribute mainly through effective interfacial-area preservation. In contrast, large-scale bubbles exhibit substantially higher *Re*, *We*, and *Eo*. Their *Re* values mainly fall within $10^2 < Re_b < 10^3$, while *We* approaches or exceeds unity in several configurations, indicating a stronger competition between inertia and surface tension. The higher *Eo* values further indicate an increased buoyancy influence. Consequently, large-scale bubbles show greater potential for interfacial deformation, wake-induced disturbance, and local interfacial renewal, although their hydrodynamic state is not uniformly inertia-dominated.

Overall, the combined multiscale bubble distributor regulates bubble size and velocity simultaneously, thereby modifying the relative roles of inertia, viscosity, buoyancy, and surface tension. Small-scale bubbles primarily favor interfacial-area preservation, whereas large-scale bubbles provide stronger transport and renewal effects. This scale-dependent hydrodynamic differentiation is summarized by the two distinct bubble clusters in the *Eo*–*Re* map shown in Figure 7.

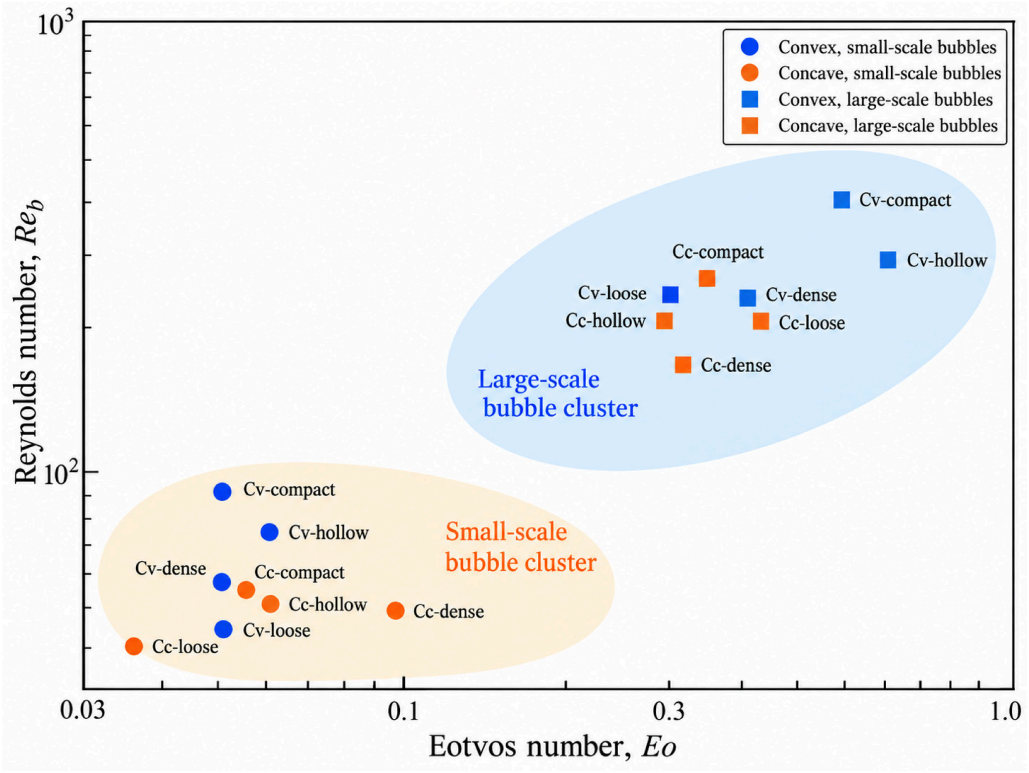


Figure 7. Eo–Re distribution of small- and large-scale bubble clusters under different configurations.

3.5. Gas–Liquid Mass Transfer Response and Synergistic Enhancement Mechanism

The gas–liquid mass-transfer performance and the scale-dependent contributions under different spatial configurations are presented in Figure 8, and error bars represent standard deviations from three independent measurements. The volumetric mass-transfer coefficient k_La reflects the combined effects of effective interfacial area and local interfacial transfer rate. Although the measured k_La values of the eight configurations remain within a relatively narrow range, the relative contributions of small- and large-scale bubbles vary markedly, indicating that spatial configuration mainly regulates the balance between interfacial-area preservation and hydrodynamic renewal rather than simply increasing the overall mass-transfer level.

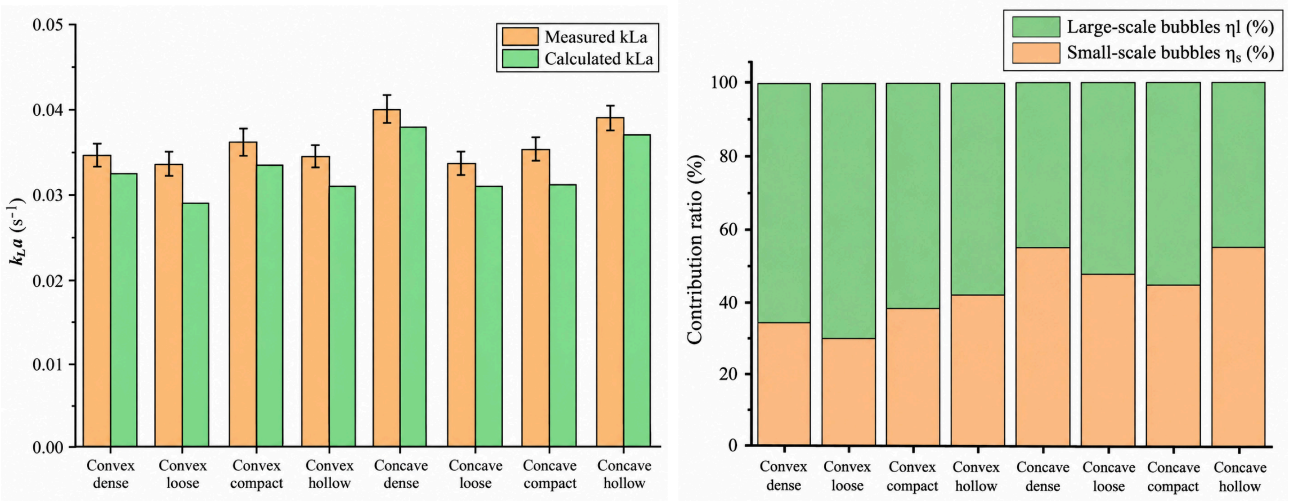


Figure 8. Gas–liquid mass transfer performance under different spatial configurations.

The measured k_La values in the present study ranged from approximately 0.032 to 0.039 s^{-1}, which are within the range reported for laboratory-scale bubble columns under low-to-moderate gas-input conditions. For example, Shah et al. and Vasconcelos et al. reported k_La values in the 10^{-2}–10^{-1} s^{-1} range depending on gas velocity and distributor conditions [2,31], whereas substantially higher values have been reported at much higher superficial gas velocities [32]. Therefore, the present k_La values are consistent in order of magnitude with representative laboratory-scale bubble-column data. More importantly, the distinctive feature of the present study is that the bubble-source composition and gas input were kept identical within each convex–concave pair, allowing the effect of vertical spatial configuration on bubble-population redistribution and scale-dependent mass-transfer contributions to be distinguished from the effect of gas throughput itself. The concave-dense and concave-hollow configurations exhibit relatively high measured k_La, whereas the convex-loose and concave-loose cases are comparatively lower. This variation does not follow the total gas flow rate or bubble velocity directly. In particular, although the convex-compact configuration shows the strongest bubble transport and the highest Re_l and We_l, its k_La does not increase proportionally. This indicates that the overall mass-transfer performance is governed by the combined effects of effective interfacial area, bubble-population structure, and hydrodynamic renewal rather than by bubble inertia alone.

The scale-resolved contribution ratios further reveal distinct mass-transfer pathways. In the convex configurations, large-scale bubbles contribute approximately 58–70% of the total scale-resolved contribution. Their higher Re_l and We_l indicate stronger transport and a greater potential for interfacial deformation and wake-related renewal, suggesting that the convex configurations are more closely associated with a large-scale-bubble hydrodynamic-renewal pathway. By contrast, the contribution of small-scale bubbles increases markedly in the concave configurations, reaching approximately 55% and 56% in the concave-dense and concave-hollow cases, respectively. Their low We_s and Eo_s indicate that surface tension strongly constrains interfacial deformation, while their smaller characteristic size favors a larger effective interfacial area per unit gas volume. The concave configurations therefore exhibit a stronger small-scale-bubble interfacial-area-preservation pathway.

Figure 9 integrates the small-scale bubble number fraction $P_s = \frac{N_s}{N_s+N_l}$, the Weber number of large-scale bubbles We_l, and the measured k_La into a structure–dynamics–mass-transfer map, where N_s and N_l are the numbers of detected small- and large-scale bubbles, respectively. Here, P_s characterizes the relative retention of small-scale bubbles and serves as an indicator of the associated interfacial-area-preservation potential, while We_l reflects the relative importance of inertia to surface tension and thus the tendency of large-scale bubbles toward interfacial deformation and hydrodynamic renewal. The marker color represents the measured overall k_La, with warmer colors indicating higher mass-transfer performance.

The convex configurations generally extend toward higher We_l, with the convex-compact case exhibiting the strongest large-scale-bubble hydrodynamic response. In contrast, most concave configurations are characterized by relatively higher P_s and lower We_l, indicating a greater tendency toward small-scale-bubble retention and interfacial-area preservation. Notably, the convex-loose configuration exhibits a high P_s without a correspondingly high k_La, whereas the convex-compact configuration shows the highest We_l but not the maximum k_La. These observations demonstrate that neither bubble-population structure nor large-scale-bubble hydrodynamics alone is sufficient to determine the overall mass-transfer performance. The hydrodynamic interpretation should be considered in relation to the active source combination rather than as a single universal convex–concave mechanism. For the dense and hollow pairs, the two 10 μm sources remain fixed at z = 0.3 m,

whereas the active 2 μm sources change their relative elevations. In the convex cases, the active outer 2 μm sources are located below the 10 μm sources, allowing the fine-bubble populations to interact with the bubble plumes initiated by the 10 μm source units during upward transport. In the corresponding concave cases, these outer fine-bubble sources are positioned above the 10 μm sources, reducing the common interaction distance. This difference is consistent with the stronger tendency toward larger bubbles and lower P_s in the convex cases and greater small-bubble retention in the corresponding concave cases. The compact pair represents a distinct interaction pattern because only the central 2 μm source is active. In the convex-compact configuration, the central fine-bubble source is positioned above the two 10 μm sources and interacts with the upward-developed bubble plumes, consistent with the strongest large-bubble hydrodynamic response observed in this case. In the concave-compact configuration, the central 2 μm source is positioned below the two 10 μm sources, resulting in a different cross-scale interaction history. The loose pair contains only the three 2 μm sources and therefore does not involve direct interaction with plumes initiated by the 10 μm source units. Its convex–concave difference is instead associated with the reversed vertical ordering of the three fine-bubble sources and the resulting differences in fine-bubble plume overlap and swarm evolution. These interpretations should be regarded as consistency-based hydrodynamic explanations supported by the measured bubble-size and velocity distributions rather than direct measurements of plume-scale interactions. Further confirmation would require time-resolved plume tracking or liquid-phase flow-field measurements.

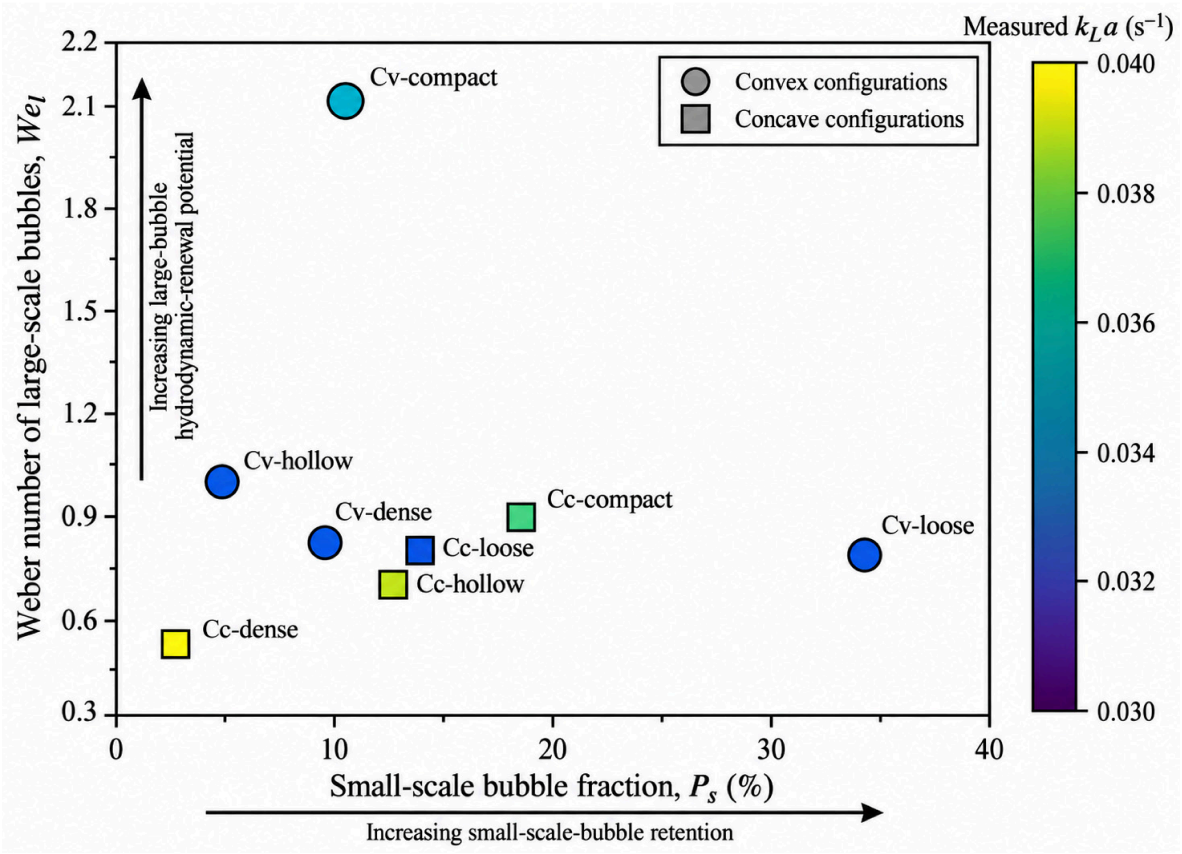


Figure 9. Structure–dynamics–mass-transfer synergy map under different spatial configurations.

Overall, spatial configuration regulates the relative contributions of small-scale-bubble retention and large-scale-bubble hydrodynamic renewal, leading to different structure–dynamics–mass-transfer states. Figure 9 therefore provides a compact representation of the

coupled relationship among bubble-population structure, scale-dependent hydrodynamics, and gas–liquid mass-transfer performance in the combined multiscale bubble system.

Beyond population-level hydrodynamic regulation, bubble–bubble and bubble–liquid interactions also involve redistribution of kinetic energy, turbulent kinetic energy, and interfacial surface energy, which can affect bubble deformation, collision/coalescence, and interfacial renewal [14,15]. In the present study, these energetic processes are reflected indirectly through the observed variations in bubble size distribution, bubble transport behavior, and scale-dependent mass-transfer contributions. However, a quantitative description of energy transfer pathways requires additional analysis combining interface-resolved simulations, population balance models, and energy-budget evaluation. Such approaches may provide further insight into the coupling among bubble interaction, energy dissipation, and gas–liquid mass transfer in spatially regulated multiscale bubble systems.

Although the present work is experimentally focused, the obtained results provide valuable benchmarks for future numerical investigations of spatially configured multiscale bubble systems. Interface-resolved methods, such as the Volume of Fluid (VOF) and level-set approaches, can be employed to investigate local bubble generation, deformation, interface evolution, and coalescence behaviors at the individual bubble scale [33]. However, fully resolved simulations of bubble-column systems remain computationally challenging due to the large number of bubbles and the wide range of spatial and temporal scales involved. For reactor-scale prediction, Eulerian–Eulerian multiphase models coupled with population balance models (PBM) provide a computationally practical framework by incorporating bubble-size distribution evolution through coalescence and breakup mechanisms [34,35]. In this context, the experimentally obtained bubble-size distributions, velocity characteristics, dimensionless parameters, and scale-dependent mass-transfer contributions in the present study can serve as experimental validation data and statistical constraints for developing multiscale numerical models of spatially regulated bubble columns.

4. Conclusions

This experimental study investigated a multiscale bubble-column system with adjustable pore-size combinations and vertical arrangements to elucidate the coupling among bubble-source composition, spatial configuration, bubble-swarm dynamics, and gas–liquid mass transfer. High-speed visualization, dimensionless analysis, and mass-transfer measurements were combined to characterize the structure–dynamics–transfer relationships. The main conclusions are as follows:

(1) The final bubble size is not directly determined by sparger pore size, but results from a continuous generation–transport–collision/coalescence–redistribution process. Even with only 2 μm-pore spargers activated, both sub-millimeter and millimeter-scale bubbles were observed, confirming the important role of swarm evolution.

(2) Spatial configuration significantly affects bubble transport. Convex arrangements generally promote stronger axial motion, with the convex-compact case exhibiting the highest velocities, whereas concave arrangements produce relatively lower and more concentrated velocity distributions. Bubble transport is therefore governed by the combined effects of gas input, size evolution, and spatial organization.

(3) Small- and large-scale bubbles exhibit distinct hydrodynamic roles in the multiscale bubble system. Small-scale bubbles contribute primarily to interfacial-area preservation, whereas large-scale bubbles enhance hydrodynamic renewal through stronger transport capability and interfacial deformation.

(4) Convex and concave configurations exhibit complementary mass-transfer pathways. Spatial configuration regulates the balance between large-scale bubble renewal and small-scale bubble retention. Convex arrangements generally enhance large-scale bub-

ble transport, whereas concave arrangements favor small-scale bubble preservation, resulting in different structure–dynamics–mass-transfer pathways.

Author Contributions: Conceptualization, L.Z.; methodology, L.Z. and J.X.; investigation, J.X.; data curation, J.X.; formal analysis, J.X.; software, J.X.; validation, J.X.; visualization, J.X.; resources, L.Z.; supervision, L.Z.; project administration, L.Z.; funding acquisition, L.Z.; writing—original draft preparation, J.X.; writing—review and editing, L.Z. and J.X. All authors have read and agreed to the published version of the manuscript.

Funding: Strategic Priority Research Program of the Chinese Academy of Sciences, "Low-carbon transformation technologies and demonstrations in chemical engineering and metallurgical processing" (Grant No. XDA0390501).

Institutional Review Board Statement: Not Applicable.

Informed Consent Statement: Not applicable.

Data Availability Statement: The original contributions presented in this study are included in the article. Further inquiries can be directed to the corresponding author.

Conflicts of Interest: The authors declare that they have no known competing financial interests or personal relationships that could have appeared to influence the work reported in this paper.

References

1. Deckwer, W.-D. *Bubble Column Reactions*; Wiley: New York, NJ, USA, 1992.
2. Shah, Y.T.; Kelkar, B.G.; Godbole, S.P.; Deckwer, W.-D. Design parameters estimations for bubble column reactors. *AIChE J.* **1982**, *28*, 353–379. [CrossRef]
3. Besagni, G.; Inzoli, F.; Ziegenhein, T. Two-Phase Bubble Columns: A Comprehensive Review. *ChemEngineering* **2018**, *2*, 13. [CrossRef]
4. Krishna, R.; van Baten, J.M. Mass transfer in bubble columns. *Catal. Today* **2003**, *79–80*, 67–75. [CrossRef]
5. Clift, R.; Grace, J.R.; Weber, M.E. *Bubbles, Drops, and Particles*; Academic Press: Cambridge, MA, USA, 1978.
6. Kulkarni, A.A.; Joshi, J.B. Bubble formation and bubble rise velocity in gas–liquid systems: A review. *Ind. Eng. Chem. Res.* **2005**, *44*, 5873–5931. [CrossRef]
7. Akita, K.; Yoshida, F. Gas holdup and volumetric mass transfer coefficient in bubble columns: Effects of liquid properties. *Ind. Eng. Chem. Process Des. Dev.* **1973**, *12*, 76–80. [CrossRef]
8. Akita, K.; Yoshida, F. Bubble size, interfacial area, and liquid-phase mass transfer coefficient in bubble columns. *Ind. Eng. Chem. Process Des. Dev.* **1974**, *13*, 84–91. [CrossRef]
9. Agarwal, A.; Ng, W.J.; Liu, Y. Principle and applications of microbubble and nanobubble technology for water treatment. *Chemosphere* **2011**, *84*, 1175–1180. [CrossRef] [PubMed]
10. Tsuge, H. *Micro- and Nanobubbles: Fundamentals and Applications*; Pan Stanford Publishing: Singapore, 2014.
11. Calderbank, P.H.; Moo-Young, M.B. The continuous phase heat and mass-transfer properties of dispersions. *Chem. Eng. Sci.* **1961**, *16*, 39–54. [CrossRef]
12. Grace, J.R.; Wairegi, T.; Nguyen, T.H. Shapes and velocities of single drops and bubbles moving freely through immiscible liquids. *Trans. Inst. Chem. Eng.* **1976**, *54*, 167–173.
13. Tomiyama, A. Struggle with computational bubble dynamics. *Multiph. Sci. Technol.* **1998**, *10*, 369–405. [CrossRef]
14. Prince, M.J.; Blanch, H.W. Bubble coalescence and break-up in air-sparged bubble columns. *AIChE J.* **1990**, *36*, 1485–1499. [CrossRef]
15. Luo, H.; Svendsen, H.F. Theoretical model for drop and bubble breakup in turbulent dispersions. *AIChE J.* **1996**, *42*, 1225–1233. [CrossRef]
16. Kulkarni, A.V.; Joshi, J.B. Design and selection of sparger for bubble column reactor. Part I: Performance of different spargers. *Chem. Eng. Res. Des.* **2011**, *89*, 1972–1985. [CrossRef]
17. Ong, B.C.; Gupta, P.; Youssef, A.; Al-Dahhan, M.; Duduković, M.P. Computed tomographic investigation of the influence of gas sparger design on gas holdup distribution in a bubble column. *Ind. Eng. Chem. Res.* **2009**, *48*, 58–68. [CrossRef]
18. Lau, R.; Sim, W.S.B.; Mo, R. Effect of gas distributor on hydrodynamics in shallow bubble column reactors. *Can. J. Chem. Eng.* **2009**, *87*, 847–854. [CrossRef]
19. Yao, Z.; Chen, C.; Wang, T.; Xia, Z.; Zhao, L.; Tang, Z.; Yan, S. Effects of gas distributor on hydrodynamics in gas–liquid bubble column by visual experiments and CFD simulations. *Chem. Eng. J.* **2025**, *504*, 158476. [CrossRef]
20. Rueda Villegas, L.; Colombet, D.; Guiraud, P.; Legendre, D.; Cazin, S.; Cockx, A. Image processing for the experimental investigation of dense dispersed flows: Application to bubbly flows. *Int. J. Multiph. Flow* **2019**, *111*, 16–30. [CrossRef]

21. Zhou, H.; Niu, X. An image processing algorithm for the measurement of multiphase bubbly flow using predictor-corrector method. *Int. J. Multiph. Flow* **2020**, *128*, 103277. [CrossRef]
22. Haas, T.; Schubert, C.; Eickhoff, M.; Pfeifer, H. BubCNN: Bubble detection using Faster R-CNN and shape regression network. *Chem. Eng. Sci.* **2020**, *216*, 115467. [CrossRef]
23. Kim, Y.; Park, H. Deep learning-based automated and universal bubble detection and mask extraction in complex two-phase flows. *Sci. Rep.* **2021**, *11*, 8940. [CrossRef] [PubMed]
24. Cerqueira, R.F.; Paladino, E.E. Development of a deep learning-based image processing technique for bubble pattern recognition and shape reconstruction in dense bubbly flows. *Chem. Eng. Sci.* **2021**, *230*, 116163. [CrossRef]
25. Hessenkemper, H.; Starke, S.; Atassi, Y.; Ziegenhein, T.; Lucas, D. Bubble identification from images with machine learning methods. *Int. J. Multiph. Flow* **2022**, *155*, 104169. [CrossRef]
26. Xu, J.; Zhou, W.; Cai, T.; Zhao, L. Multi-scale bubble flow and mass transfer visual measurements in real time aid with deep learning method. *Int. J. Multiph. Flow* **2026**, *195*, 105507. [CrossRef]
27. Han, C.; Guan, X.; Yang, N. Structure Evolution and Demarcation of Small and Large Bubbles in Bubble Columns. *Ind. Eng. Chem. Res.* **2018**, *57*, 8529–8540. [CrossRef]
28. Li, C.; Cui, Y.; Shi, X.; Gao, J.; Lan, X. Numerical Simulation on the Terminal Rise Velocity and Mass Transfer Rate of Single Sub-Millimeter Bubbles. *Chem. Eng. Sci.* **2021**, *246*, 116963. [CrossRef]
29. Higbie, R. The rate of absorption of a pure gas into a still liquid during short periods of exposure. *Trans. AIChE* **1935**, *31*, 365–389.
30. Alves, S.S.; Orvalho, S.P.; Vasconcelos, J.M.T. Effect of bubble contamination on rise velocity and mass transfer. *Chem. Eng. Sci.* **2004**, *59*, 3837–3843. [CrossRef]
31. Vasconcelos, J.M.T.; Rodrigues, J.M.L.; Orvalho, S.C.P.; Alves, S.S.; Mendes, R.L.; Reis, A. Effect of contaminants on mass transfer coefficients in bubble column and airlift contactors. *Chem. Eng. Sci.* **2003**, *58*, 1431–1440. [CrossRef]
32. McClure, D.D.; Kavanagh, J.M.; Fletcher, D.F.; Barton, G.W. Oxygen transfer in bubble columns at industrially relevant superficial velocities: Experimental work and CFD modelling. *Chem. Eng. J.* **2015**, *280*, 138–146. [CrossRef]
33. Hirt, C.W.; Nichols, B.D. Volume of Fluid (VOF) Method for the Dynamics of Free Boundaries. *J. Comput. Phys.* **1981**, *39*, 201–225. [CrossRef]
34. Wang, T. Simulation of Bubble Column Reactors Using CFD Coupled with a Population Balance Model. *Front. Chem. Sci. Eng.* **2011**, *5*, 162–172. [CrossRef]
35. Bhole, M.R.; Joshi, J.B.; Ramkrishna, D. CFD Simulation of Bubble Columns Incorporating Population Balance Modeling. *Chem. Eng. Sci.* **2008**, *63*, 2267–2282. [CrossRef]

Disclaimer/Publisher's Note: The statements, opinions and data contained in all publications are solely those of the individual author(s) and contributor(s) and not of MDPI and/or the editor(s). MDPI and/or the editor(s) disclaim responsibility for any injury to people or property resulting from any ideas, methods, instructions or products referred to in the content.